

Multiphysics Simulation of Nucleation and Grain Growth in Selective Laser Melting of Alloys

Dehao Liu

Woodruff School of Mechanical Engineering,
Georgia Institute of Technology,
Atlanta, GA 30332
e-mail: dehao.liu@gatech.edu

Yan Wang¹

Woodruff School of Mechanical Engineering,
Georgia Institute of Technology,
Atlanta, GA 30332
e-mail: yan.wang@me.gatech.edu

Selective laser melting (SLM) builds parts by selectively melting metallic powders layer by layer with a high-energy laser beam. It has a variety of applications in aerospace, medical device, and other low-volume manufacturing. Nevertheless, the lack of fundamental understanding of the process-structure-property relationship for better quality control inhibits wider applications of SLM. Recently, a mesoscale simulation approach, called phase field and thermal lattice Boltzmann method (PF-TLBM), was developed to simulate microstructure evolution of alloys in SLM melt pool with simultaneous consideration of solute transport, heat transfer, phase transition, and latent heat effect. In this paper, a nucleation model is introduced in the PF-TLBM framework to simulate heterogeneous nucleation at the boundary of the melt pool in SLM. A new method is also developed to estimate the thermal flux out of the SLM melt pool model given a constant cooling rate. The effects of latent heat and cooling rate on dendritic morphology and solute distribution are studied. The simulation results of AlSi10Mg alloy suggest that the inclusion of latent heat is necessary because it reveals the details of the formation of secondary arms, reduces the overestimation of microsegregation, and provides more accurate kinetics of dendritic growth. [DOI: 10.1115/1.4046543]

Keywords: selective laser melting, nucleation, dendritic growth, phase field method, thermal lattice Boltzmann method, computational foundations for additive manufacturing, multiphysics modeling and simulation

1 Introduction

As a powder bed-based additive manufacturing (AM) technique, selective laser melting (SLM) builds three-dimensional (3D) parts by melting layers of fine-grained metallic powders with a laser beam. It significantly improves the manufacturability of complex geometries and heterogeneous materials. SLM has the potential to be widely applied in various industries including automotive, aerospace, biomedical, energy, and other high-value low-volume manufacturing environments. However, the lack of fundamental understanding of the process-structure-property (P-S-P) relationship of SLM becomes the bottleneck to produce defect-free, structurally sound, and reliable AM parts. There is a critical need to understand the rapid solidification process during which microstructures are formed and the properties of solid parts are determined.

During the complex process of solidification, interactions between solute transport, heat transfer, and phase transition have significant effects on the formation of the microstructure. The final solidified microstructure determines the mechanical strength, thermal conductivity, corrosion resistance, and other properties of the AM parts. A thorough understanding of the rapid solidification process allows us to establish the P-S-P relationship for process design and optimization. Establishing the P-S-P relationship in high-dimensional parameter space requires a large number of samples. Currently, the capabilities of in situ observation for rapid solidification at the nano- and micro-scales are very limited. Compared with experimental studies, simulation is more cost-effective to reveal the cause-effect relations. Multiscale multiphysics simulation sometimes becomes the only viable approach to study complex phenomena.

Various models have been developed to understand and predict microstructure evolution during solidification. These include front-tracking, enthalpy, level-set, cellular automaton (CA), and phase field method (PFM) [1]. Particularly, PFM and CA are the most used methods. CA is computationally much more efficient than PFM so that it can be applied to simulate large systems. However, PFM [2,3] can reveal more details of dendritic growth dynamics and side branch emission. CA predictions of anisotropic gain structures are sensitive to the choice of mesh shapes. The dendrite tip velocities predicted by PFM agree with the Lipton-Glicksman-Kurz model more than CA simulations [4].

PFM has been widely used to simulate dendritic growth in the solidification processes of casting, welding, and AM [5–7]. Recently, more comprehensive models to simulate complex physical phenomena have been developed. For instance, multicomponent multiphase field model coupled with thermodynamic databases can simulate alloys more accurately [8]. Materials related properties required for PFM such as interface energy and interface mobility can be predicted from molecular dynamics when experimental data are limited [9]. Other numerical schemes such as mesh free method [10] have also been explored to improve the numerical robustness from conventional finite element and finite difference methods.

The rapid solidification in AM is a highly complex process where it is not appropriate to make equilibrium assumptions of the thermal field and melt flow. A multiphysics simulation approach is necessary to understand the coupling effects among temperature, velocity, and phase fields. Some multiphysics models that combine CA or PFM with other physics, including fluids and thermal, have been developed. For instance, a 3D cellular automata finite volume method [11] was used to predict the grain growth of IN718 alloy inside the melt pool during AM processes. A cellular automata lattice Boltzmann method [12,13] was proposed to simulate the grain texture evolution in the selective melting. Finite element analysis has been widely employed to obtain the geometry and thermal history of the melt pool, which can be used in the

¹Corresponding author.

Manuscript received October 17, 2019; final manuscript received February 21, 2020; published online March 2, 2020. Assoc. Editor: Mahesh Mani.

subsequent PFM simulation of dendritic growth [14–18]. Computational fluid dynamics analysis and PFM were also combined to simulate the dendritic growth in the melt pool [19]. In addition, phase field and lattice Boltzmann method (PF-LBM) [20–23] has been widely used to simulate dendritic growth in melt flows where LBM simulates single-phase and multiphase flows with complex boundary conditions and multiphase interfaces. In our previous work [24–26], a phase field and thermal lattice Boltzmann method (PF-TLBM) was developed to investigate the effects of latent heat and forced melt flow on the dendritic morphology, concentration, and temperature field during SLM process. The simulation results of Ti-6Al-4V showed that the consideration of nonequilibrium temperature field and latent heat in addition to melt flows is very necessary, because it reveals the details of the formation of secondary arms and provides more realistic kinetics of dendritic growth.

In this work, the PF-TLBM is extended to include a nucleation model for heterogeneous nucleation and dendritic growth. Nucleation affects the accuracy of simulated microstructures in SLM, but it has only been considered in few studies of PFM simulation. Shimono et al. [27] simulated the columnar-to-equiaxed transition (CET) of Ti-6Al-4V alloy during the AM process by coupling PFM with the calculation of phase diagrams (CALPHAD). A continuous Gaussian nucleation distribution was used to describe the grain density increase with the increase in undercooling. The empirical nucleation parameters, such as maximum nucleation density and mean undercooling, were calibrated based on experimental results. However, this empirical model missed some important physics of nucleation compared with classical nucleation theory (CNT). Gránásy et al. [28,29] described two methods to include homogeneous nucleation into PFM simulations. In the first method, Langevin noise terms were introduced in PFM as a nucleation force. In the second one, the nucleation energy barrier was determined by solving the Euler–Lagrange equations of the phase field and composition field. PFM was also used to determine the nucleation energy barrier for heterogeneous nucleation, where appropriate boundary conditions were introduced at the foreign wall to realize the required contact angle [30]. Pusztai et al. [31] introduced Langevin noise terms in PFM to simulate homogeneous and heterogeneous nucleation in polycrystalline. However, by introducing Langevin noises, nucleation could occur anywhere in the simulation domain rather than the solid–liquid interface because of the nature of stochastic partial differential equations. The model works well for large melt pools such as in casting, but not accurate in SLM with small melt pools. In powder-based SLM, the size of the melt pool is usually less than 100 μm . Furthermore, it is known that nucleation and growth occur at different time scales, the observation of nucleation would require an impractically large number of sample frequencies and integration cycles. Therefore, Simmons et al. [32] replaced the Langevin noise terms in PFM with a Poisson seeding algorithm, where viable nuclei were introduced at a time-dependent nucleation rate. However, the developed model is used for homogeneous nucleation rather than heterogeneous nucleation. In the work of Li et al. [33], the nucleation kinetics of binary melts is calculated based on CNT. The model was originally used to simulate polycrystalline solidification of NiCu alloy in casting, where the clear CET was clearly shown. However, the heterogeneous nucleation in the model occurred in the melt pool rather than the boundary of the melt pool. In SLM, heterogeneous nucleation tends to occur at the solid–liquid interface at the bottom of the small melt pool as experimentally observed.

In this study, a nucleation model is introduced into the PF-TLBM framework for simulating the microstructure evolution of alloys in SLM. AlSi10Mg alloy is used to demonstrate the simulation framework. AlSi10Mg alloy, with good weldability, hardenability and high dynamic properties, have been widely applied in automotive and aerospace industries. The main contribution of this work is the simulation of nucleation and dendritic growth of alloys in the small melt pool of SLM, where heterogeneous nucleation tends to occur at the boundary. A method to approximate the thermal flux

out of the small melt pool for PF-TLBM is also developed, given a constant cooling rate.

In the remainder of this paper, the formulation of PF-TLBM and the new nucleation model are described in Sec. 2. The simulation settings of the SLM melt pool, simulation results of AlSi10Mg alloy, and the effects of latent heat and cooling rate on dendritic growth are shown in Sec. 3. The quantitative analyses of thermal history, the time evolution of solid-phase fraction, and composition distribution are also provided.

2 Methodology

In this section, the formulation of PF-TLBM is briefly described. The PFM formulation is introduced in Sec. 2.1. The thermal lattice Boltzmann method (TLBM) is introduced in Sec. 2.2. More details about PF-TLBM can be found in Ref. [25]. The phase field and composition are calculated by solving the Allen–Cahn equation and diffusion equation. The temperature field is obtained from TLBM. PFM and TLBM are tightly coupled by updating and exchanging the information of phase, composition, and temperature fields in each iteration of the simulation. In Sec. 2.3, the new nucleation model is described, which is used to simulate the heterogeneous nucleation in the mushy zone of the melt pool in the SLM process.

2.1 Phase Field Method. The multiphase field method [2,21] is used to describe the liquid–solid phase transition during the solidification process. The main advantage of PFM is that the movement of the interface of the microstructure is tracked implicitly rather than explicitly. In PFM, a continuous variable named phase field ϕ is used to keep track of the solid-phase fraction in the simulated domain. The microstructure evolution is modeled by the time evolution of the phase field.

The kinetic equation for the phase field is given by

$$\frac{\partial \phi}{\partial t} = M_\phi \left\{ \sigma^*(\mathbf{n}) \left[\nabla^2 \phi + \frac{\pi^2}{\eta^2} \left(\phi - \frac{1}{2} \right) \right] + \frac{\pi}{\eta} \sqrt{\phi(1-\phi)} \Delta G_V \right\} \quad (1)$$

where M_ϕ is the effective interface mobility, η is the interface width, and $\mathbf{n} = \nabla \phi / |\nabla \phi| = (n_x, n_y)$ is the local normal direction of the interface. The anisotropic interface energy stiffness is defined as

$$\sigma^* = \sigma + \frac{\partial^2 \sigma}{\partial \psi^2} = \sigma \tilde{\sigma} [1 - 3\delta + 4\delta(n_x^4 + n_y^4)] \quad (2)$$

where σ is the interface energy, $\psi = \arctan(n_y/n_x)$ indicates the grain orientation, $\sigma \tilde{\sigma}$ is the prefactor of interface energy stiffness, and δ is the anisotropy strength of interface energy stiffness. The driving force is described by

$$\Delta G_V = \Delta S(T_m - T + m_l C_l) \quad (3)$$

where $\Delta S = L_H \rho / T_l$ is the entropy difference between solid and liquid phases, L_H is the latent heat of fusion, ρ is the density, T_l is the liquidus temperature, T_m is the melting temperature of pure material, T is the current temperature, m_l represents the liquidus slope, and C_l represents the weight percentage (wt%) of solute in the liquid phase.

The kinetic equation for the composition field is given by

$$\frac{\partial C}{\partial t} = \nabla \cdot [D_l(1-\phi)\nabla C_l] + \nabla \cdot \mathbf{j}_{at} \quad (4)$$

where $C = \phi C_s + (1-\phi)C_l$ is the overall composition of a solute in the simulation domain and C_s is the composition of the solid phase. During rapid solidification, the dynamic partition coefficient can be calculated according to Aziz's model [34]

$$k = \frac{C_s}{C_l} = \frac{k_e + V_l \lambda / D_l}{1 + V_l \lambda / D_l} \quad (5)$$

where k_e is the equilibrium partition coefficient, λ is the actual width of the interface in atomic dimensions, and V_I is the interface velocity. The diffusion coefficient of the liquid phase is given by

$$D_l = D_0 \exp\left(\frac{-\Delta E}{RT}\right) \quad (6)$$

where D_0 is the prefactor of diffusion coefficient of liquid phase, ΔE is activation energy, and R is gas constant. The anti-trapping current is introduced and defined as

$$\mathbf{j}_{at} = \frac{\eta}{\pi} \sqrt{\phi(1-\phi)}(C_l - C_s) \frac{\partial \phi}{\partial t} \frac{\nabla \phi}{|\nabla \phi|} \quad (7)$$

which is used to remove the unphysical solute trapping caused by the finite interface width.

The driving force is not calculated based on the phase diagram in the equilibrium state. The reasons are listed as follows. The driving force is determined by the current temperature and composition field. The temperature evolution is simulated by TLBM, whereas the composition field is computed by Fick's law during rapid solidification. Both the partition coefficient and diffusion coefficient of the liquid phase are not constant. The dynamic partition coefficient varies with the interface velocity. The diffusion coefficient of the liquid phase varies with the temperature. Although the calculation of the driving force is not as accurate as CALPHAD computation [35], it is more efficient.

2.2 Thermal Lattice Boltzmann Method. In this work, the melt is assumed to be static in the small pool for simplification. The effect of Marangoni flow on dendritic growth will be considered in future work. TLBM [36,37] is used to calculate the temperature field only in this study. TLBM is used to simulate the temperature evolution in the melt pool and consider the effects of the release of latent heat at the solid-liquid interface.

The heat conduction equation is given by

$$\frac{\partial T}{\partial t} = \nabla \cdot (\alpha \nabla T) + \dot{q} \quad (8)$$

where α is the thermal diffusivity. The released latent heat during solidification is given by

$$\dot{q} = \frac{L_H}{c_p} \frac{\partial \phi}{\partial t} \quad (9)$$

where c_p is the specific heat capacity. Instead of solving Eq. (8) directly, a particle distribution function of temperature $g_i(\mathbf{x}, t)$ is utilized to capture the dynamics of the system in TLBM. Particles move dynamically between neighboring discretized lattice nodes in TLBM. In a two-dimensional D2Q9 scheme, each node has eight neighbors. The velocity vector along the i th direction in the lattice with respect to a reference node is given by

$$\mathbf{e}_i = \begin{cases} (0, 0), & i = 0 \\ (\pm c, 0), (0, \pm c), & i = 1, \dots, 4 \\ (\pm c, \pm c), & i = 5, \dots, 8 \end{cases} \quad (10)$$

where $c = \Delta x / \Delta t$ is the lattice velocity with grid spacing Δx and time-step Δt , and index i corresponds to a unique direction in the lattice. The kinetic equation of particle distribution of temperature is given by

$$g_i(\mathbf{x} + \mathbf{e}_i \Delta t, t + \Delta t) = g_i(\mathbf{x}, t) + \frac{1}{\tau_g} [g_i^{eq}(\mathbf{x}, t) - g_i(\mathbf{x}, t)] + Q_i(\mathbf{x}, t) \Delta t \quad (11)$$

where $\tau_g = 3\alpha / (c^2 \Delta t) + 0.5$ is the dimensionless relaxation time, $g_i^{eq}(\mathbf{x}, t) = \omega_i T$ is the equilibrium distribution, and

$$Q_i = \left(1 - \frac{1}{2\tau_g}\right) \omega_i \dot{q} \quad (12)$$

is the heat source term. In the D2Q9 scheme, the weights ω_i 's associated with direction i 's are

$$\omega_i = \begin{cases} 4/9, & i = 0 \\ 1/9, & i = 1, \dots, 4 \\ 1/36, & i = 5, \dots, 8 \end{cases} \quad (13)$$

During each iteration, the temperature T can be calculated from the particle distribution of temperature g_i 's as

$$T = \sum_i g_i + \frac{\Delta t}{2} \dot{q} \quad (14)$$

In the SLM process, heat transfer is much faster than solute diffusion because thermal diffusivity can be three to four orders of magnitude larger than solute diffusivity. In order to improve the computational efficiency, a fine grid spacing dx is used for the PFM simulation, whereas a coarse grid spacing $\Delta x = 50 dx$ is used for the TLBM simulation. The same time-step Δt is used for both simulations. The results of TLBM are linearly interpolated as the input for the PFM model, whereas the results of PFM are averaged and transferred to the TLBM model in each iteration. The anti-bounceback scheme [38,39] is used for the thermal boundary condition. The particle distribution of temperature at the boundary node $g_i(\mathbf{x}_b, t + \Delta t)$, for direction \bar{i} such that $\mathbf{e}_{\bar{i}} = -\mathbf{e}_i$, is determined by

$$g_{\bar{i}}(\mathbf{x}_b, t + \Delta t) = -g_i(\mathbf{x}_b, t) - \frac{1}{\tau_g} [g_i^{eq}(\mathbf{x}_b, t) - g_i(\mathbf{x}_b, t)] + 2\omega_i T_w \quad (15)$$

The temperature of the wall T_w is given by

$$T_w = T_b - \frac{q_H \Delta x}{2\kappa} \quad (16)$$

where T_b is the temperature at the boundary node, q_H is the outward heat flux at the boundary, and κ is the thermal conductivity of the material.

2.3 Nucleation Model. During the SLM process, columnar dendrites grow from the bottom of the melt pool upward, as usually observed in experiments. Heterogeneous nucleation usually has a much lower energy barrier than homogeneous

Table 1 Physical properties of AlSi10Mg alloy

Physical properties	Value
The melting point of pure Al, T_m (K)	933 [35]
Liquidus temperature, T_l (K)	867 [41]
Solidus temperature, T_s (K)	831 [41]
Liquidus slope, m_l (K/wt%)	-6.6 [35]
Equilibrium partition coefficient, k_e	0.104 [35]
Prefactor of interface energy stiffness, σ_0^* (J/m ²)	0.169 [42]
Interfacial energy stiffness anisotropy, δ	0.27 [42]
Interface mobility, M_ϕ (m ⁴ /(J · s))	1×10^{-8} [43]
Entropy difference, ΔS (J/(m ³ · K))	1.3×10^6
Physical interface width, λ (m)	3×10^{-9} [44]
Prefactor of diffusion coefficient of liquid phase, D_0 (m ² /s)	1.34×10^{-7} [45]
Activation energy, ΔE (J/mol)	3×10^4 [45]
Kinematic viscosity, ν (m ² /s)	4.87×10^{-7} [41]
Thermal diffusivity, α (m ² /s)	4.5×10^{-5} [41]
Thermal conductivity, κ (W/(m · K))	110 [41]
Latent heat of fusion, L_H (J/kg)	4.23×10^5 [41]
Specific heat capacity, c_p (J/(kg · K))	915 [41]
Density, ρ (kg/m ³)	2670 [41]
Heat transfer coefficient, h (W/(m ² · K))	82 [46]
Emissivity, ε	0.4 [46]

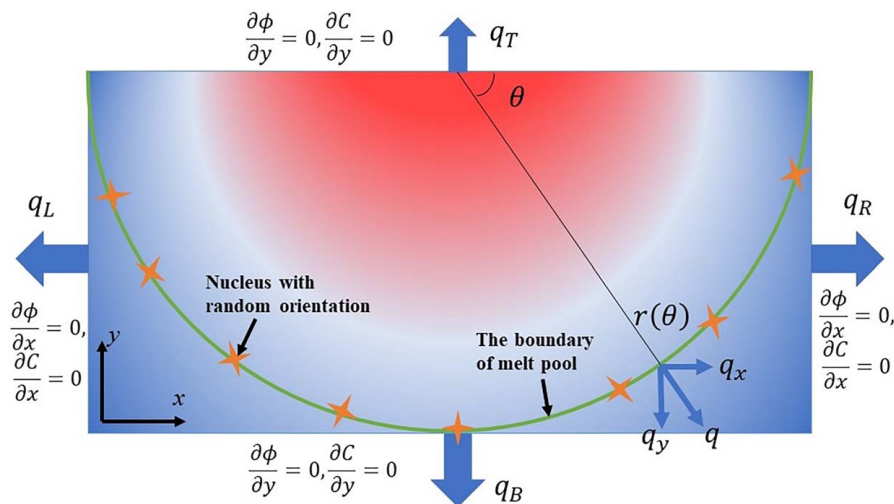


Fig. 1 Schematic diagram of the setup of boundary conditions

nucleation. Therefore, it is reasonable to assume that heterogeneous nucleation dominates and nuclei concentrate at the solid–liquid interface. To simulate the heterogeneous nucleation process, a Poisson seeding algorithm [32,33] is adopted. Nucleation can be treated as fully localized events and can be modeled as a Poisson process. The major assumption is the spatial and temporal independence between events with the memoryless property. The nucleation probability is given by

$$P_n = 1 - \exp(-I\nu\Delta t) \quad (17)$$

where I is the nucleation rate, ν is the cell spacing, and Δt is a sufficiently small time interval. Based on the CNT, the nucleation rate can be calculated by

$$I = I_0 \exp\left[-\frac{16\pi\sigma^3 f(\bar{\theta})}{3kT(\Delta G_V)^2}\right] \quad (18)$$

where $I_0 \approx 1 \times 10^{16} \text{ m}^{-2}/\text{s}$ is the prefactor of the nucleation rate determined by the jump frequency across the interface, σ is the interface energy, $f(\bar{\theta}) = (2 - 3 \cos \bar{\theta} + \cos^3 \bar{\theta})/4 = 1 \times 10^{-5}$ with $\bar{\theta}$ as the contact angle, k is the Boltzmann constant, ΔG_V is the driving force in Eq. (3). The prefactor of the nucleation rate for AlSi10Mg alloy is calibrated based on the average β grain size observed in the SLM experiment [40], which is $5 \mu\text{m}$. During each time-step, the nucleation probability P_n is calculated at each liquid cell at the boundary of the melt pool during the simulation. At the same time, a random number with the standard uniform distribution between 0 and 1 will be generated and compared with the nucleation probability P_n . If the random number is less than the nucleation probability P_n , then the nucleus is planted.

3 Results and Discussion

In this section, the simulation setup and the simulation results are described. The effects of latent heat and cooling rate on the dendritic growth of AlSi10Mg alloy in the melt pool are studied. The quantitative analyses of thermal history, the time evolution of solid-phase fraction, and composition distribution are also provided.

3.1 Computational Setup. The PF-TLBM framework is used to simulate nucleation and dendritic growth of AlSi10Mg alloy in the melt pool during the SLM process. In AlSi10Mg alloy, the composition of Si is high (9–11 wt%) and the composition of Mg is low

(0.2–0.45 wt%). Therefore, it is reasonable to assume the main solute of AlSi10Mg alloy is Si. By using the pseudo-binary approach, the ternary AlSi10Mg alloy is treated as a binary alloy, and the solute is the combination of Si and Mg. The physical properties of AlSi10Mg alloy are listed in Table 1 [35,41–46]. For simplification, most properties of AlSi10Mg except the diffusivity of liquid phase are assumed to be temperature independent during solidification. The dependence of physical properties on temperature needs to be considered to further improve prediction accuracy in future work. The algorithm is implemented in c++ programming language and integrated with the open-source software OPENPHASE.² PFM and lattice Boltzmann method (LBM) have been implemented in the original OPENPHASE. The OpenMP shared-memory parallel programming framework is used to accelerate the computation. There are three main contributions and new features in our implementation. First, LBM has been extended as TLBM so that heat transfer can be simulated. Second, a probabilistic nucleation model has been introduced in the framework. Finally, a double-mesh scheme has been implemented to improve computational efficiency of the multiphysics model.

Since thermal diffusivity is three to four orders of magnitude larger than solute diffusivity, a double-mesh scheme is adopted in simulations to reduce computational cost. A fine grid spacing $dx = 0.2 \mu\text{m}$ is used for the PFM simulation, whereas a coarse grid spacing $\Delta x = 50 dx = 10 \mu\text{m}$ is used for the TLBM simulation. Based on the stability analysis, the upper limit of the time-step should be $\Delta t \leq \min\{dx^2/(4D_l), \Delta x^2/(4\nu), \Delta x^2/(4\alpha)\}$. As a result, the time-step $\Delta t = 0.2 \mu\text{s}$ is applied in all simulation runs. The experimental results show that the width and depth of the melt pool in SLM of AlSi10Mg are $100 \mu\text{m}$ [40]. Therefore, the length and width of the two-dimensional simulation domain as the cross section of the melt pool are chosen to be $L_x = L_y = 500 dx = 100 \mu\text{m}$. The interface width is $\eta = 5 dx$, meaning that there are six nodes on the interface or boundary layer. The initial composition of the solute is set as $C_0 = 10 \text{ wt}\%$ for the whole simulation domain. The initial temperature is $T_0 = 867 \text{ K}$ for the whole simulation domain.

The setup of boundary conditions for simulations is schematically illustrated in Fig. 1. The rectangular region stands for the cross section of the melt pool, which is perpendicular to the scanning direction. The curve indicates the boundary of the melt pool, where nuclei with random distributions are generated. Zero Neumann conditions are set at all boundaries for the phase field ϕ and composition C .

²<http://www.openphase.de/>

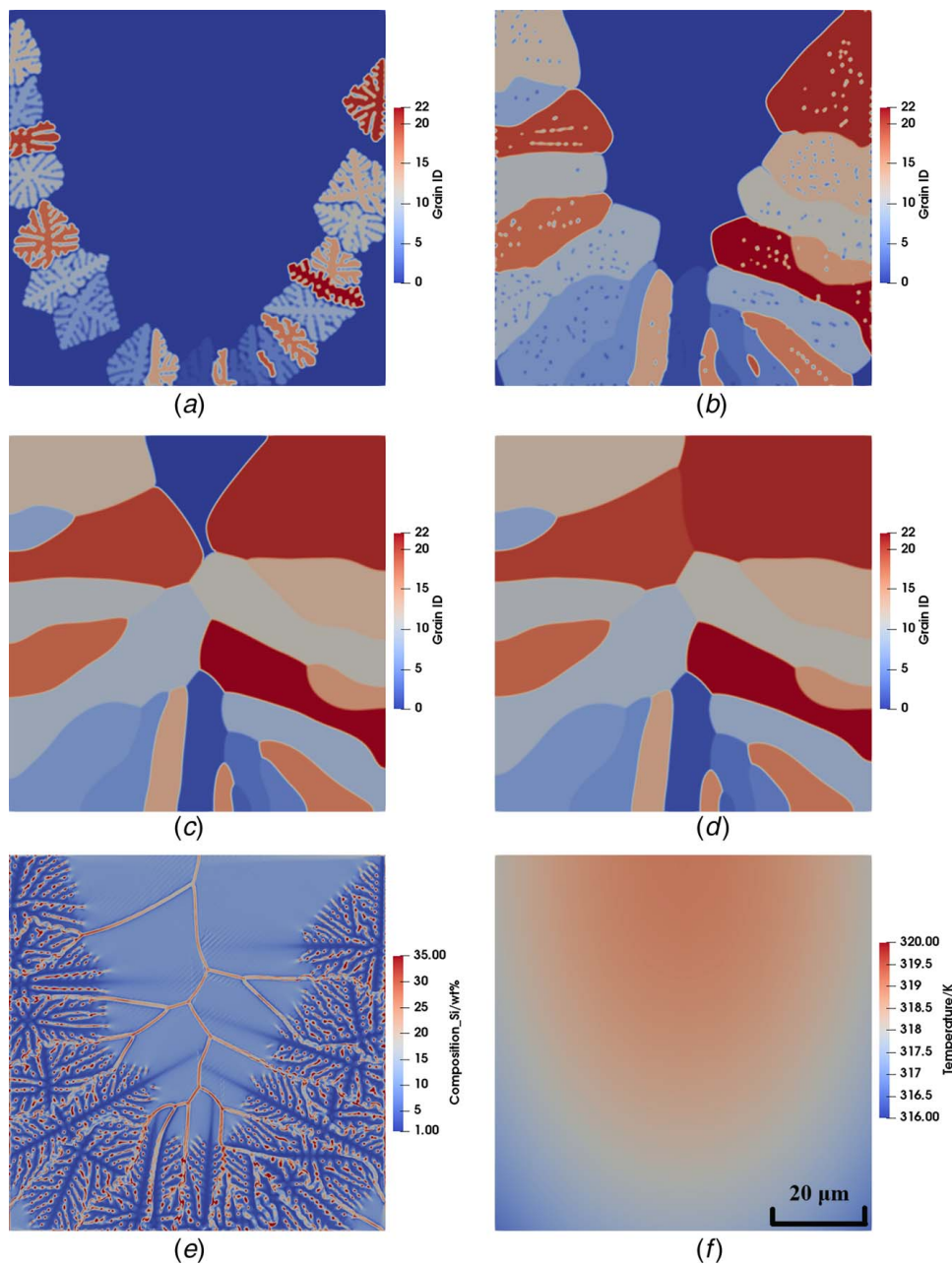


Fig. 2 Dendritic growth without latent heat when $\dot{T} = 5 \times 10^4$ K/s: (a) phase field at 2.8 ms, (b) phase field at 5.6 ms, (c) phase field at 8.4 ms, (d) phase field at 11.2 ms, (e) composition field at 11.2 ms, and (f) temperature field at 11.2 ms

In all simulations, constant cooling rates are applied in an indirect way. It is noted that the nonisothermal solidification in the melt pool is simulated by applying heat fluxes at boundaries rather than cooling the whole simulation domain at a constant cooling rate. First, four constant heat fluxes q_T , q_B , q_L , and q_R are calculated based on a constant cooling rate. Then, these four heat fluxes q_T , q_B , q_L , and q_R are applied at the top, bottom, left, and right boundaries, respectively. The relationship between a constant cooling rate and heat fluxes at the boundaries need to be established so that the solidification in the melt pool is nonisothermal to reflect the real situation. Three heat fluxes q_B , q_L , and q_R are estimated based on their geometric relation to the heat flux \mathbf{q} which is normal to the boundary of the melt pool. More specifically, \mathbf{q} is decomposed into three heat fluxes q_B , q_L , and q_R . It is assumed that the heat flux \mathbf{q} has a constant magnitude. It is necessary to determine the relationship between heat fluxes q_B , q_L , and q_R so that the magnitude of heat fluxes at boundaries can be calculated. To make it

more general, it is assumed that the shape of the melt pool is a semi-ellipse, which is defined as

$$r(\theta) = (a \cos \theta, b \sin \theta) \quad (19)$$

where a is the major axis, b is the minor axis, and θ is an angular parameter that defines the position. The heat flux \mathbf{q} normal to the boundary of the melt pool has a constant magnitude and is given by

$$\mathbf{q} = q\mathbf{N} = \frac{q}{\sqrt{a^2 \sin^2 \theta + b^2 \cos^2 \theta}} (b \cos \theta, a \sin \theta) \quad (20)$$

where \mathbf{N} is the unit normal vector perpendicular to the boundary of the melt pool. It is obvious that the heat flux \mathbf{q} can be decomposed to $\mathbf{q}_x = q/\sqrt{a^2 \sin^2 \theta + b^2 \cos^2 \theta} (b \cos \theta, 0)$ and $\mathbf{q}_y = q/\sqrt{a^2 \sin^2 \theta + b^2 \cos^2 \theta} (0, a \sin \theta)$. Because the semi-ellipse is symmetric with respect to the y -axis, let us consider the case

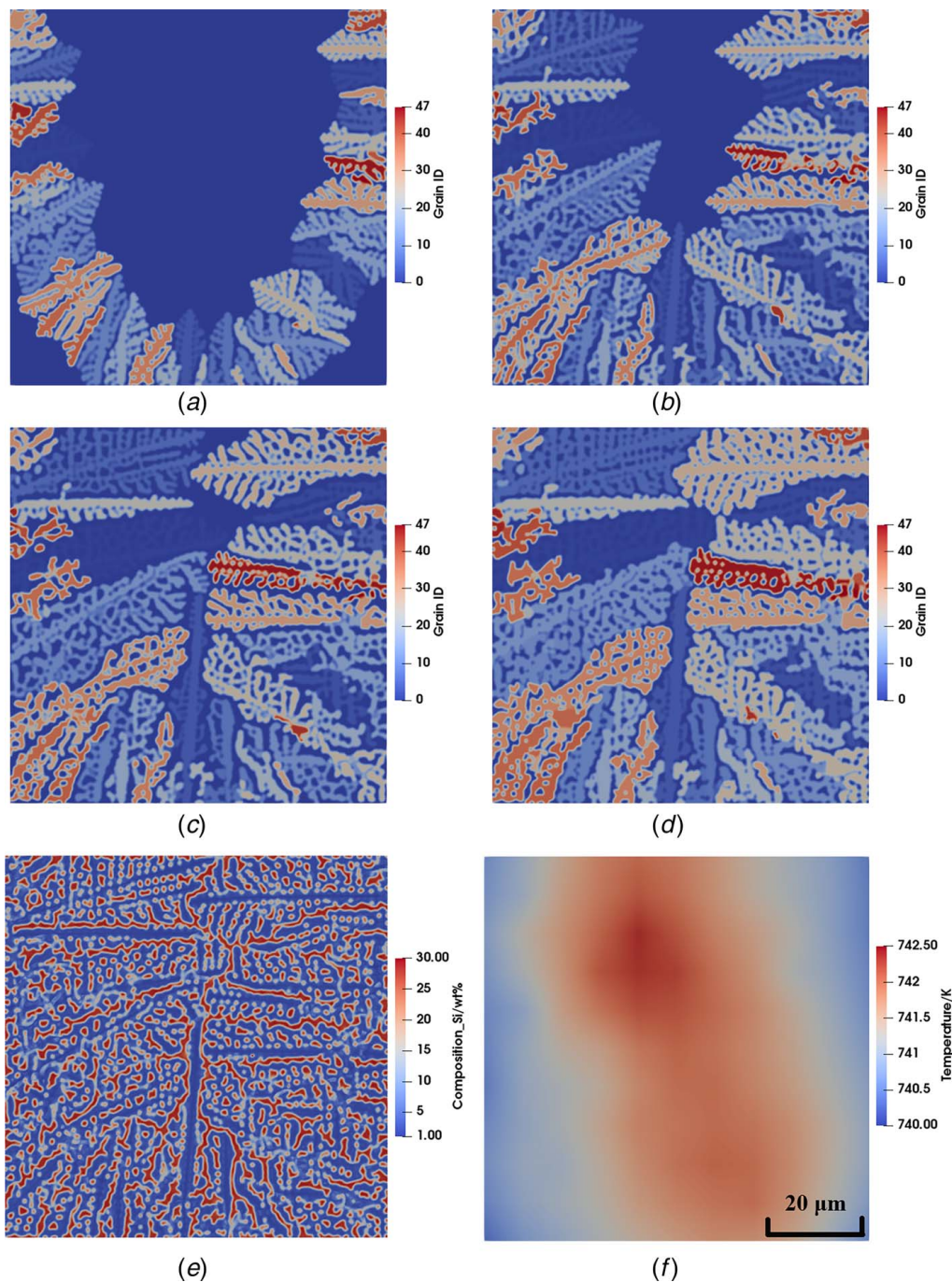


Fig. 3 Dendritic growth with latent heat when $\dot{T} = 5 \times 10^4$ K/s: (a) phase field at 4 ms, (b) phase field at 8 ms, (c) phase field at 12 ms, (d) phase field at 16 ms, (e) composition field at 16 ms, and (f) temperature field at 16 ms

when $-\pi/2 \leq \theta \leq \pi/2$ first. By using vector calculus, the rate of heat flow caused by the horizontal heat flux \mathbf{q}_x can be calculated by

$$\dot{Q}_x = \int_{-\pi/2}^{\pi/2} \mathbf{q}_x \cdot \mathbf{N} ds = \int_{-\pi/2}^{\pi/2} \mathbf{q}_x \cdot \mathbf{N} |r'(\theta)| d\theta = \int_{-\pi/2}^{\pi/2} \frac{qb^2 \cos^2 \theta}{\sqrt{a^2 \sin^2 \theta + b^2 \cos^2 \theta}} d\theta \quad (21)$$

Similarly, the rate of heat flow caused by the vertical heat flux \mathbf{q}_y is given by

$$\dot{Q}_y = \int_{-\pi/2}^{\pi/2} \mathbf{q}_y \cdot \mathbf{N} ds = \int_{-\pi/2}^{\pi/2} \mathbf{q}_y \cdot \mathbf{N} |r'(\theta)| d\theta = \int_{-\pi/2}^{\pi/2} \frac{qa^2 \sin^2 \theta}{\sqrt{a^2 \sin^2 \theta + b^2 \cos^2 \theta}} d\theta \quad (22)$$

Both \dot{Q}_x and \dot{Q}_y can be calculated by numerical integration. On the other hand, from the definition of rate of heat flow, we have

$$\frac{\dot{Q}_x}{\dot{Q}_y} = \frac{q_R L_y}{q_B L_x / 2} \quad (23)$$

Because of the symmetry of the melt pool, the rates of heat flow at the left and right boundaries are the same, as

$$q_L L_y = q_R L_y \quad (24)$$

For all simulations in this work, the length and width of the simulation domain are the same. Therefore, the ratio between the rates of

heat flow along the x -direction and y -direction can be computed by numerical integration of Eqs. (21) and (22) as

$$\frac{\dot{Q}_x}{\dot{Q}_y} = \frac{2q_R L_y}{q_B L_x} = \frac{2q_R}{q_B} \approx 2.84 \quad (25)$$

Based on Eqs. (24) and (25), a relationship can be derived as

$$q_L = q_R = 1.42q_B \quad (26)$$

The heat flux at the top boundary caused by the convection and radiation heat transfer is defined as [46]

$$q_T = h(T_l - T_0) + \sigma_{SB}\epsilon(T_l^4 - T_0^4) \quad (27)$$

where σ_{SB} is Stefan–Boltzmann constant and $T_0 = 298$ K is room temperature. Given a constant cooling rate \dot{T} , the other three heat fluxes q_B , q_L , and q_R can be calculated based on the energy balance equation [47]

$$L_x L_y \rho c_p \dot{T} = q_T L_x + q_B L_x + q_L L_y + q_R L_y \quad (28)$$

After four heat fluxes are obtained, the temperature of the wall T_w can be updated in each iteration based on Eq. (16).

3.2 Dendritic Growth Without Latent Heat. The dendritic growth of AlSi10Mg alloy is first simulated without the release of latent heat for comparison. A constant cooling rate $\dot{T} = 5 \times 10^4$ K/s is used. The simulation results are shown in Fig. 2. The grain identification (ID) 0 represents the liquid phase, whereas other grain IDs represent solid phases with different orientations. During the rapid solidification process, the columnar dendritic growth dominates in the melt pool, as shown in Fig. 2.

At the time of 2.8 ms, the columnar dendritic growth pattern is observed, as shown in Fig. 2(a). The primary arms and secondary arms still can be differentiated. As a result of the anisotropy of interface energy, the primary arms grow faster than secondary arms. Since the release of latent heat is ignored, the secondary arms grow so fast that they quickly merge with each other as shown in Fig. 2(b). At the time of 11.2 ms, the melt has been completely solidified as shown in Fig. 2(d). The composition field at 11.2 ms is shown in Fig. 2(e), where primary arms and secondary arms can be differentiated easily. The microsegregation occurs at the grain boundaries and the small pockets between secondary arms. In Fig. 2(f), the temperature at the upper center of the melt pool is the highest, which is caused by the setup of heat fluxes at the boundaries. Since the primary arms aligned with the temperature gradient grow faster than those do not, this results in the radial distribution pattern of columnar dendrites in the melt pool, as shown in Fig. 2(d). Since the latent heat is ignored, the temperature decreases so fast that it approaches room temperature at 11.2 ms as shown in Fig. 2(f). This observation does not agree well with the experimental evidence, which also indicates the significance of considering the release of latent heat.

3.3 Dendritic Growth With Latent Heat. In the second case, the dendritic growth with the release of latent heat is simulated. The cooling rate is also kept as $\dot{T} = 5 \times 10^4$ K/s. Figure 3 shows the simulation results. At the time of 4 ms, a clear dendritic growth pattern is shown in Fig. 3(a), where primary arms and secondary arms can be differentiated easily. When the dendrites continue to grow, the primary arms aligned with the temperature gradient grow faster than those do not as shown in Figs. 3(b)–3(d). However, there is still some residual melt between grains. The melt is not completely solidified even at the time of 16 ms, as shown in Fig. 3(d). The composition field at 16 ms is shown in Fig. 3(e), where secondary arms can still be observed clearly. The small pockets of the liquid phase at grain boundaries may remain liquid for a long period of time until solid diffusion takes away the remaining solute supersaturation before it is

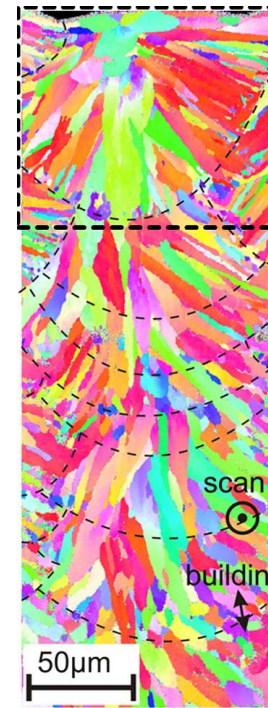


Fig. 4 Experimental EBSD result of the grain texture in the cross section of the AlSi10Mg sample produced by SLM (courtesy of Thijs et al. [40]).

completely solidified. The microsegregation at grain boundaries in the case with latent heat is lower than that in the case without latent heat. Figure 3(f) shows the temperature field at 16 ms. The temperature in the case with latent heat is higher than that in the case without latent heat. The maximum temperature (742.5 K) is lower than the temperature of solidus (831 K) in equilibrium. However, the melt is not completely solidified. This is because the actual solidus temperature during nonequilibrium solidification is lower than that in the equilibrium case. This observation agrees with the CALPHAD results in the work of Marola et al. [35]. Based on the above comparison, the inclusion of latent heat is very necessary because it reveals the details of the formation of secondary arms.

The simulated grain structure in Fig. 3(d) qualitatively matches the experimental observation by electron backscatter diffraction (EBSD) [40] in Fig. 4. After one laser pass, the dendrites at the curved boundary of the melt pool will grow and result in a radial distribution pattern. The cross section of the AlSi10Mg sample by SLM in the top layer is highlighted with a dashed rectangle. The secondary arm spacing of the simulated dendrite is $\lambda_2 = 1.1 \mu\text{m}$, which is close to the calculated value $\lambda_2 = 0.6 \mu\text{m}$ based on the analytical model developed by Bouchard and Kirkaldy [48], as

$$\lambda_2 = 12\pi \left[\frac{4\sigma D_l^2}{C_0(1-k)^2 \rho L_H V_f^2} \right]^{1/3} \quad (29)$$

The difference between the predicted and observed secondary arm spacing could be caused by parameter uncertainty and model-form uncertainty. The parameter uncertainty can be associated with the interface energy σ , latent heat L_H , solute diffusivity D_l , and local velocity of the interface V_f .

3.4 The Effect of Cooling Rate. In order to investigate the effect of cooling rate on dendritic morphology and composition distribution, a higher cooling rate $\dot{T} = 1 \times 10^5$ K/s is used. The release

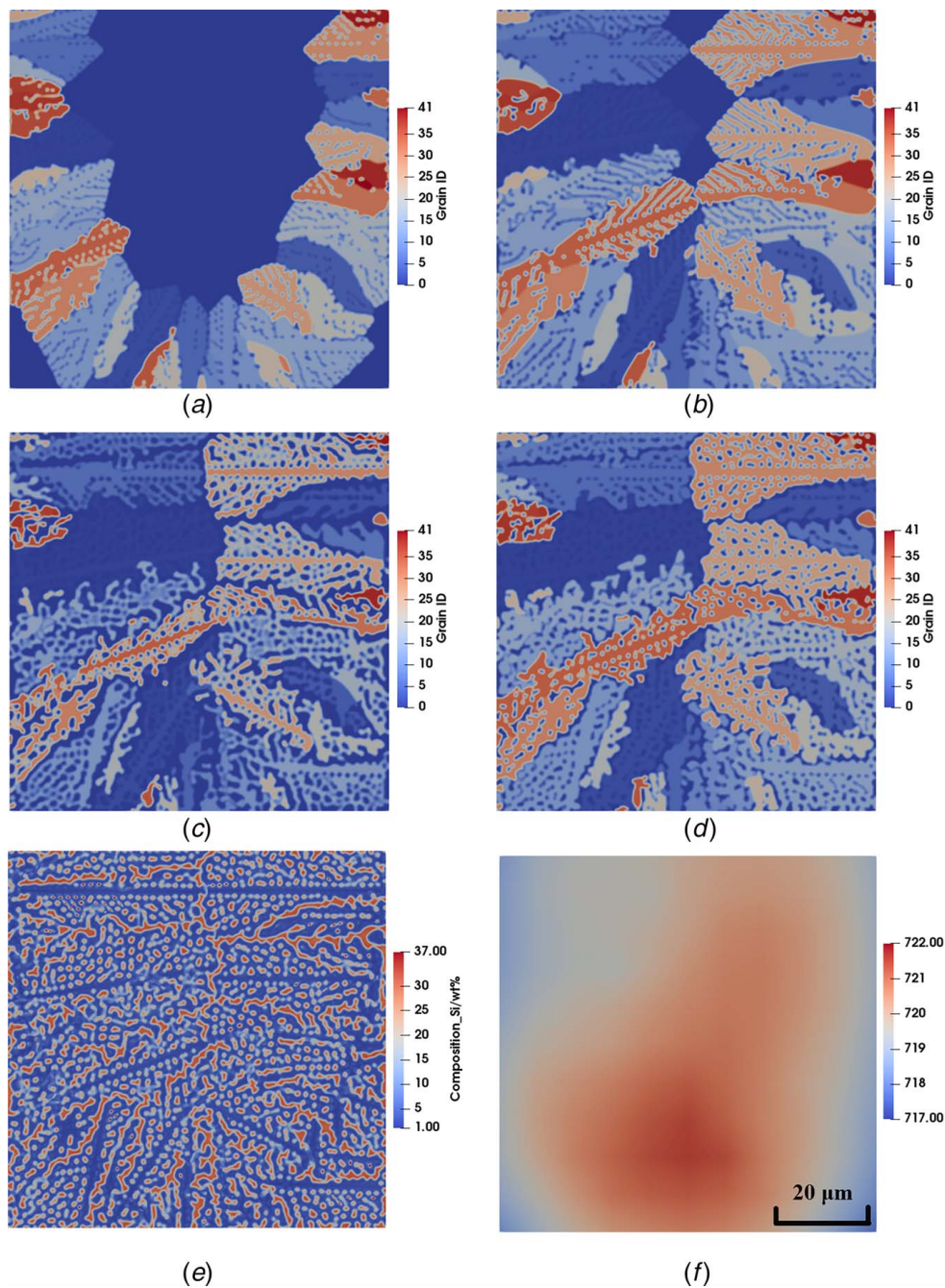


Fig. 5 Dendritic growth with latent heat when $\dot{T} = 1 \times 10^5$ K/s: (a) phase field at 4 ms, (b) phase field at 8 ms, (c) phase field at 12 ms, (d) phase field at 16 ms, (e) composition field at 16 ms, and (f) temperature field at 16 ms

of latent heat is included in this case. The simulation results are presented in Fig. 5. It is observed that the growth velocity of dendrites increases with the cooling rate. As a result, the secondary arms merge with each other and disappear. The melt is almost completely solidified at the time of 16 ms as shown in Fig. 5(d). Because of the competitive growth of different grains, a small grain is merged with its neighbor grain, which is highlighted in a dashed rectangle, as shown in Fig. 5. The final grain structure in Fig. 5(d) is different from those in Figs. 2(d) and 3(d) because the increased cooling rate influences the competitive growth of dendrites. The rising cooling rate also increases the microsegregation at grain boundaries, as shown in Fig. 5(e). Figure 5(f) shows that the temperature is lower than that in the case with the cooling rate $\dot{T} = 5 \times 10^4$ K/s in Fig. 3(f).

3.5 Quantitative Analysis. In this section, a quantitative analysis is conducted to compare the effects of latent heat and cooling rate on temperature field, dendritic morphology, and composition field. Figure 6 shows the thermal histories at the location of $x = 50 \mu\text{m}$, $y = 50 \mu\text{m}$ for the simulated three situations. When the release of latent heat is not considered, the temperature decreases linearly. When the release of latent heat is considered and the nominal cooling rate is $\dot{T} = 5 \times 10^4$ K/s, the temperature drops quasilinearly at the beginning of solidification ($0 \leq t < 4$ ms). Since the fraction of phase transition is small at the beginning, the effect of latent heat is not obvious. When $t \geq 4$ ms, the temperature starts to increase until 10 ms and then decreases again. This phenomenon is widely known as recalescence during the solidification of alloys. When the cooling rate is increased to $\dot{T} = 1 \times 10^5$ K/s, the effect of

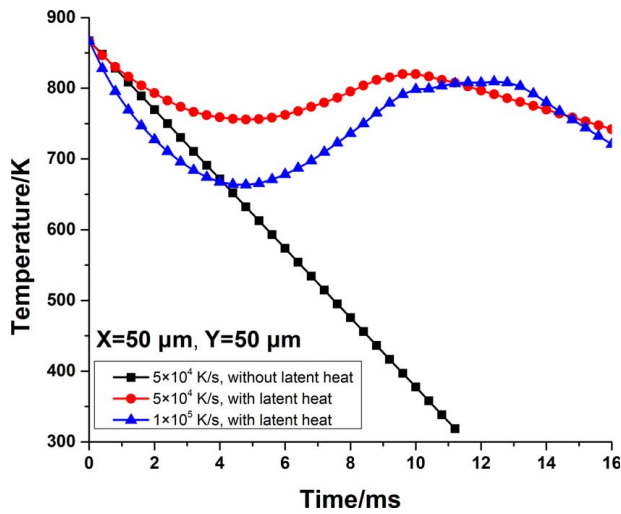


Fig. 6 Thermal histories at the location of $x = 50 \mu\text{m}$, $y = 50 \mu\text{m}$ under different conditions

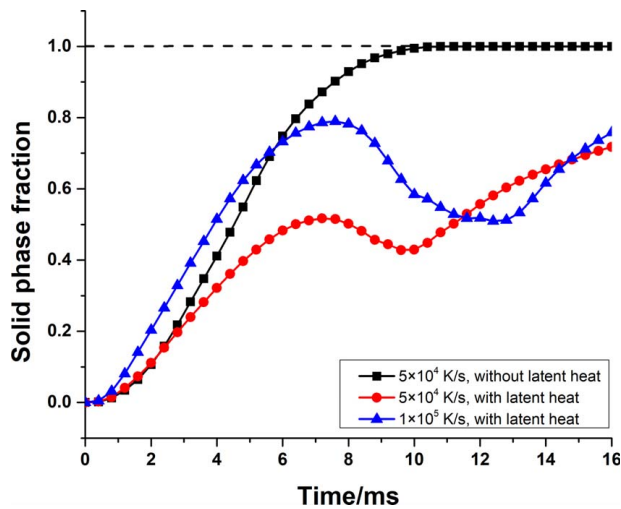


Fig. 7 Histories of solid-phase fractions under different conditions

latent heat on the temperature field is reduced. The temperature drops quasi-linearly at the beginning of solidification ($0 \leq t < 4$ ms) and it is lower than that in the case of $\dot{T} = 5 \times 10^4$ K/s. When $t \geq 4$ ms, the temperature starts to increase until 13 ms, and then decreases again.

The histories of the solid-phase fractions for different cases are shown in Fig. 7. Here, the solid-phase fraction means the total fraction of solid phases in the simulation domain. When solid-phase fraction equals to one, the melt is completely solidified. When the latent heat is ignored, the history curve of solid-phase fraction looks like an “S”-shaped logistic sigmoid function, which increases slowly at the beginning, then increases rapidly and reaches plateaus near the end. The solid-phase fraction reaches 1.0 at the time of 11 ms, meaning that the liquid–solid phase transition is finished. When the latent heat is considered and the nominal cooling rate is $\dot{T} = 5 \times 10^4$ K/s, the solid fraction increases at the beginning, then decreases and increases again. This means the remelting happens during rapid solidification because of the release of latent heat. The solid-phase fraction is 0.72 at the time of 16 ms. It will take some additional time to finish the solidification process because of the release of latent heat and microsegregation in small pockets. When the cooling rate increases to $\dot{T} = 1 \times 10^5$ K/s, the speed of phase transition increases and the solid fraction is 0.76 at the time of 16 ms.

The composition distributions at the location of $y = 50 \mu\text{m}$ at the time of 11.2 ms without latent heat and 16 ms with latent heat are shown in Fig. 8. It is observed that the locations where microsegregation occurs are mostly the same for different cases. The microsegregation can be defined as

$$\chi = \frac{C_{\max}}{C_{\min}} \quad (30)$$

where C_{\max} is the maximum of composition, and C_{\min} is the minimum of composition. When the latent heat is ignored, the microsegregation is overestimated, which is $\chi = 45.44/1.27 = 35.78$. When the latent heat is considered and the nominal cooling rate is $\dot{T} = 5 \times 10^4$ K/s, there are more secondary arms and peaks of microsegregation. The microsegregation is $\chi = 29.5/1.1 = 26.82$. Therefore, the microsegregation without the latent heat is overestimated by at least 33% compared with that with the latent heat. When the cooling increases to $\dot{T} = 1 \times 10^5$ K/s, the microsegregation is $\chi = 37.14/1.2 = 30.95$.

Based on the above quantitative analysis, the inclusion of latent heat is important because it provides more realistic kinetics of dendritic growth and reduces overestimated microsegregation. The increased cooling rate increases the speed of phase transition and microsegregation.

In this study, all simulations were run using eight processors with Intel Xeon Processor E5-2680 (2.50 GHz) and memories of 16 GB. It took 41 h and 31 min for simulating 11.2 ms of the case in Sec. 3.2, 48 h and 22 min for 16 ms of the case in Sec. 3.3, and 48 h and 42 min for 16 ms of the case in Sec. 3.4.

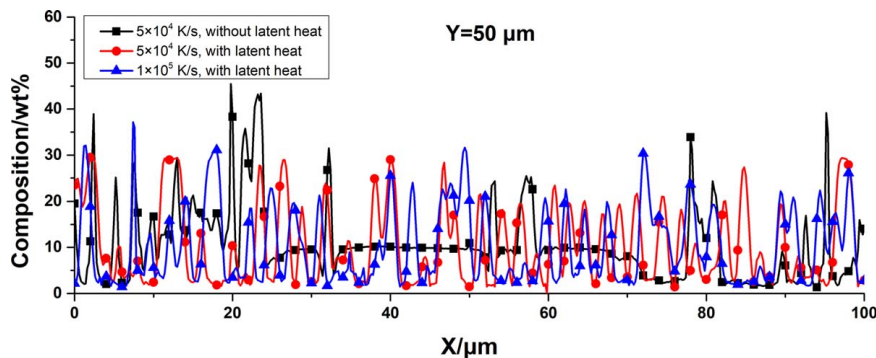


Fig. 8 Composition distributions at the location of $y = 50 \mu\text{m}$ at the time of 11.2 ms without latent heat and 16 ms with latent heat

4 Conclusions

In this work, a nucleation model is introduced into the recently developed PF-TLBM framework to consider the heterogeneous nucleation process at the solid–liquid interface. This mesoscale multiphysics model is used to simulate the nucleation and dendritic growth of AlSi10Mg alloy in the SLM melt pool. A new method is proposed to estimate the thermal flux for a 2D small melt pool in order to approximate the actual nonisothermal temperature field in SLM. The simultaneous considerations of solute transport, heat transfer, nucleation, and dendritic growth are necessary to understand complex rapid solidification in SLM. By considering the release of latent heat, the model is able to predict the temperature field, composition distribution, and dendritic morphology with more details than models without latent heat. The recalescence occurs when the latent heat is considered. The qualitative and quantitative analyses show that the inclusion of latent heat is necessary because it reveals the details of the formation of secondary arms, reduces the overestimation of microsegregation, and provides more realistic kinetics of dendritic growth. A higher cooling rate results in faster liquid–solid-phase transition and higher microsegregation at grain boundaries.

Further work is needed to improve the fidelity, accuracy, and efficiency of the PF-TLBM model. For instance, the surface tension source term could be introduced into the TLBM so that the effect of Marangoni flow on dendritic growth can be investigated. The motion of grains can be enabled as well. Furthermore, the empirical nucleation parameters need to be determined and calibrated based on experimental measurements, first-principles calculations, or atomistic simulations. The determination of the nucleation energy barrier or nucleation rate can help to predict a more realistic microstructure. The dependence of physical properties of AlSi10Mg alloy on temperature needs to be considered to improve prediction accuracy, which can be found in the work of Pei et al. [46]. The model-form and parameter uncertainties associated with the developed model should be quantified to provide more confidence in the prediction. A parallelized 3D PF-TLBM is needed to simulate the dendritic growth in the melt pool with more details. Both the PFM and the TLBM can be modified for parallel computation without much difficulty.

The proposed mesoscale multiphysics PF-TLBM model is a key component in a multiscale simulation framework for SLM processes, which involves multiple and complex physical phenomena. It predicts the microstructure evolution in the SLM process at a reasonable time scale. The predicted microstructure is the central hinge of the P-S-P relationship, which needs to be investigated for process design and optimization. Classical continuum simulation methods cannot provide fine-grained material phase and composition distribution, whereas atomistic models cannot simulate the time scales which are long enough for manufacturing processes.

Acknowledgment

This work is supported in part by the George W. Woodruff Faculty Fellowship at the Georgia Institute of Technology.

References

- [1] Jaafar, M. A., Rousse, D. R., Gibout, S., and Bédécarrats, J. P., 2017, “A Review of Dendritic Growth During Solidification: Mathematical Modeling and Numerical Simulations,” *Renewable Sustainable Energy Rev.*, **74**, pp. 1064–1069.
- [2] Steinbach, I., 2009, “Phase-Field Models in Materials Science,” *Modell. Simul. Mater. Sci. Eng.*, **17**(7), p. 073001.
- [3] Steinbach, I., 2013, “Why Solidification? Why Phase-Field?,” *JOM*, **65**(9), pp. 1096–1102.
- [4] Choudhury, A., Reuther, K., Wesner, E., August, A., Nestler, B., and Rettenmayr, M., 2012, “Comparison of Phase-Field and Cellular Automaton Models for Dendritic Solidification in Al-Cu Alloy,” *Comput. Mater. Sci.*, **55**, pp. 263–268.
- [5] Boettinger, W. J., Warren, J. A., Beckermann, C., and Karma, A., 2002, “Phase Field Simulation of Solidification,” *Annu. Rev. Mater. Res.*, **32**(1), pp. 63–94.

- [6] Chen, L.-Q., 2002, “Phase-Field Models for Microstructure Evolution,” *Annu. Rev. Mater. Res.*, **32**(1), pp. 113–140.
- [7] Moelans, N., Blanpain, B., and Wollants, P., 2008, “An Introduction to Phase-Field Modeling of Microstructure Evolution,” *CALPHAD: Comput. Coupling Phase Diagrams Thermochem.*, **32**(2), pp. 268–294.
- [8] Böttger, B., Eiken, J., and Steinbach, I., 2006, “Phase Field Simulation of Equiaxed Solidification in Technical Alloys,” *Acta Mater.*, **54**(10), pp. 2697–2704.
- [9] Fu, Y., Michopoulos, J. G., and Song, J. H., 2017, “Bridging the Multi Phase-Field and Molecular Dynamics Models for the Solidification of Nano-Crystals,” *J. Comput. Sci.*, **20**, pp. 187–197.
- [10] Song, J. H., Fu, Y., Kim, T. Y., Yoon, Y. C., Michopoulos, J. G., and Rabczuk, T., 2018, “Phase Field Simulations of Coupled Microstructure Solidification Problems via the Strong Form Particle Difference Method,” *Int. J. Mech. Mater. Des.*, **14**(4), pp. 491–509.
- [11] Lian, Y., Gan, Z., Yu, C., Kats, D., Liu, W. K., and Wagner, G. J., 2019, “A Cellular Automaton Finite Volume Method for Microstructure Evolution During Additive Manufacturing,” *Mater. Des.*, **169**, p. 107672.
- [12] Körner, C., Attar, E., and Heintz, P., 2011, “Mesoscopic Simulation of Selective Beam Melting Processes,” *J. Mater. Process. Technol.*, **211**(6), pp. 978–987.
- [13] Rai, A., Markl, M., and Körner, C., 2016, “A Coupled Cellular Automaton–Lattice Boltzmann Model for Grain Structure Simulation During Additive Manufacturing,” *Comput. Mater. Sci.*, **124**, pp. 37–48.
- [14] Liu, P. W., Ji, Y. Z., Wang, Z., Qiu, C. L., Antonyasamy, A. A., Chen, L. Q., Cui, X. Y., and Chen, L., 2018, “Investigation on Evolution Mechanisms of Site-Specific Grain Structures During Metal Additive Manufacturing,” *J. Mater. Process. Technol.*, **257**, pp. 191–202.
- [15] Wang, X., and Chou, K., 2019, “Microstructure Simulations of Inconel 718 During Selective Laser Melting Using a Phase Field Model,” *Int. J. Adv. Manuf. Technol.*, **100**(9–12) pp. 2147–2162.
- [16] Keller, T., Lindwall, G., Ghosh, S., Ma, L., Lane, B. M., Zhang, F., Kattner, U. R., Lass, E. A., Heigel, J. C., Idell, Y., Williams, M. E., Allen, A. J., Guyer, J. E., and Levine, L. E., 2017, “Application of Finite Element, Phase-Field, and CALPHAD-Based Methods to Additive Manufacturing of Ni-Based Superalloys,” *Acta Mater.*, **139**, pp. 244–253.
- [17] Liu, P., Wang, Z., Xiao, Y., Horstemeyer, M. F., Cui, X., and Chen, L., 2019, “Insight Into the Mechanisms of Columnar to Equiaxed Grain Transition During Metallic Additive Manufacturing,” *Addit. Manuf.*, **26**, pp. 22–29.
- [18] Yang, Y., Ragnvaldsen, O., Bai, Y., Yi, M., and Xu, B. X., 2019, “3D Non-Isothermal Phase-Field Simulation of Microstructure Evolution During Selective Laser Sintering,” *npj Comput. Mater.*, **5**(1), pp. 1–12.
- [19] Acharya, R., Sharon, J. A., and Staroselsky, A., 2017, “Prediction of Microstructure in Laser Powder Bed Fusion Process,” *Acta Mater.*, **124**, pp. 360–371.
- [20] Medvedev, D., and Kassner, K., 2005, “Lattice Boltzmann Scheme for Crystal Growth in External Flows,” *Phys. Rev. E Stat. Nonlin. Soft Matter Phys.*, **72**(5), pp. 1–10.
- [21] Medvedev, D., Varnik, F., and Steinbach, I., 2013, “Simulating Mobile Dendrites in a Flow,” *Procedia Comput. Sci.*, **18**, pp. 2512–2520.
- [22] Takaki, T., Rojas, R., Ohno, M., Shimokawabe, T., and Aoki, T., 2015, “GPU Phase-Field Lattice Boltzmann Simulations of Growth and Motion of a Binary Alloy Dendrite,” *IOP Conference Series: Materials Science and Engineering*, **84**, p. 012066.
- [23] Rojas, R., Takaki, T., and Ohno, M., 2015, “A Phase-Field-Lattice Boltzmann Method for Modeling Motion and Growth of a Dendrite for Binary Alloy Solidification in the Presence of Melt Convection,” *J. Comput. Phys.*, **298**, pp. 29–40.
- [24] Liu, D., and Wang, Y., 2017, “Mesoscale Multi-Physics Simulation of Solidification in Selective Laser Melting Process Using a Phase Field and Thermal Lattice Boltzmann Model,” 2017 ASME International Design Engineering Technical Conferences & The Computer and Information in Engineering Conference (IDETC/CIE2017), Cleveland, OH, Aug. 6–9, p. DETC2017-67633.
- [25] Liu, D., and Wang, Y., 2019, “Mesoscale Multi-Physics Simulation of Rapid Solidification of Ti-6Al-4V Alloy,” *Addit. Manuf.*, **25**, pp. 551–562.
- [26] Liu, D., and Wang, Y., 2019, “Simulation of Nucleation and Grain Growth in Selective Laser Melting of Ti-6Al-4V Alloy,” 2019 ASME International Design Engineering Technical Conferences & The Computer and Information in Engineering Conference (IDETC/CIE2019), Anaheim, CA, ASME, p. DETC2019-97684.
- [27] Shimono, Y., Oba, M., Nomoto, S., Koizumi, Y., and Chiba, A., 2017, “Numerical Simulation of Solidification in Additive Manufacturing of Ti Alloy by Multi-Phase Field Method,” *Solid Freeform Fabrication Symposium*, Austin, TX, Aug. 7–9, pp. 1048–1057.
- [28] Gránásy, L., Börzsönyi, T., and Pusztai, T., 2002, “Crystal Nucleation and Growth in Binary Phase-Field Theory,” *J. Cryst. Growth*, **237–239**(1–4), pp. 1813–1817.
- [29] Gránásy, L., Börzsönyi, T., Börzsönyi, T., and Pusztai, T., 2002, “Nucleation and Bulk Crystallization in Binary Phase Field Theory,” *Phys. Rev. Lett.*, **88**(20), p. 206105.
- [30] Gránásy, L., Pusztai, T., Saylor, D., and Warren, J. A., 2007, “Phase Field Theory of Heterogeneous Crystal Nucleation,” *Phys. Rev. Lett.*, **98**(3), p. 035703.
- [31] Pusztai, T., Tegze, G., Tóth, G. I., Környei, L., Bansel, G., Fan, Z., and Grínsy, L., 2008, “Phase-Field Approach to Polycrystalline Solidification Including Heterogeneous and Homogeneous Nucleation,” *J. Phys. Condens. Matter*, **20**(40), p. 404205.

- [32] Simmons, J. P., Wen, Y., Shen, C., and Wang, Y. Z., 2004, "Microstructural Development Involving Nucleation and Growth Phenomena Simulated With the Phase Field Method," *Mater. Sci. Eng. A*, **365**(1–2), pp. 136–143.
- [33] Li, J., Wang, J., and Yang, G., 2007, "Phase-Field Simulation of Microstructure Development Involving Nucleation and Crystallographic Orientations in Alloy Solidification," *J. Cryst. Growth*, **309**(1), pp. 65–69.
- [34] Aziz, M. J., 1982, "Model for Solute Redistribution During Rapid Solidification," *J. Appl. Phys.*, **53**(2), pp. 1158–1168.
- [35] Marola, S., Manfredi, D., Fiore, G., Poletti, M. G., Lombardi, M., Fino, P., and Battezzati, L., 2018, "A Comparison of Selective Laser Melting With Bulk Rapid Solidification of AlSi10Mg Alloy," *J. Alloys Compd.*, **742**, pp. 271–279.
- [36] Chen, S., and Doolen, G. D., 1998, "Lattice Boltzmann Method for Fluid Flows," *Annu. Rev. Fluid Mech.*, **30**(1), pp. 329–364.
- [37] Guo, Z., Zheng, C., Shi, B., and Zhao, T. S., 2007, "Thermal Lattice Boltzmann Equation for Low Mach Number Flows: Decoupling Model," *Phys. Rev. E Stat. Nonlin. Soft Matter Phys.*, **75**(3), p. 036704.
- [38] Zhang, T., Shi, B., Guo, Z., Chai, Z., and Lu, J., 2012, "General Bounce-Back Scheme for Concentration Boundary Condition in the Lattice-Boltzmann Method," *Phys. Rev. E—Stat. Nonlin. Soft Matter Phys.*, **85**(1), p. 016701.
- [39] Chen, Q., Zhang, X., and Zhang, J., 2013, "Improved Treatments for General Boundary Conditions in the Lattice Boltzmann Method for Convection-Diffusion and Heat Transfer Processes," *Phys. Rev. E*, **88**(3), p. 033304.
- [40] Thijs, L., Kempen, K., Kruth, J. P., and Van Humbeeck, J., 2013, "Fine-Structured Aluminium Products With Controllable Texture by Selective Laser Melting of Pre-Alloyed AlSi10Mg Powder," *Acta Mater.*, **61**(5), pp. 1809–1819.
- [41] Mukherjee, T., Wei, H. L., De, A., and DebRoy, T., 2018, "Heat and Fluid Flow in Additive Manufacturing—Part II: Powder Bed Fusion of Stainless Steel, and Titanium, Nickel and Aluminum Base Alloys," *Comput. Mater. Sci.*, **150**, pp. 369–380.
- [42] Napolitano, R. E., Liu, S., and Trivedi, R., 2002, "Experimental Measurement of Anisotropy in Crystal-Melt Interfacial Energy," *Interface Sci.*, **10**(2–3), pp. 217–232.
- [43] Steinbach, I., 2008, "Effect of Interface Anisotropy on Spacing Selection in Constrained Dendrite Growth," *Acta Mater.*, **56**(18), pp. 4965–4971.
- [44] Hoyt, J. J., Asta, M., and Karma, A., 2003, "Atomistic and Continuum Modeling of Dendritic Solidification," *Mater. Sci. Eng. R: Reports*, **41**(6), pp. 121–164.
- [45] Du, Y., Chang, Y. A., Huang, B., Gong, W., Jin, Z., Xu, H., Yuan, Z., Liu, Y., He, Y., and Xie, F. Y., 2003, "Diffusion Coefficients of Some Solutes in Fcc and Liquid Al: Critical Evaluation and Correlation," *Mater. Sci. Eng. A*, **363**(1–2), pp. 140–151.
- [46] Pei, W., Zhengying, W., Zhen, C., Junfeng, L., Shuzhe, Z., and Jun, D., 2017, "Numerical Simulation and Parametric Analysis of Selective Laser Melting Process of AlSi10Mg Powder," *Appl. Phys. A: Mater. Sci. Process.*, **123**(8), pp. 1–15.
- [47] Loginova, I., Amberg, G., and Ågren, J., 2001, "Phase-Field Simulations of Non-Isothermal Binary Alloy Solidification," *Acta Mater.*, **49**(4), pp. 573–581.
- [48] Bouchard, D., and Kirkaldy, J. S., 1996, "Equations and Specification of Predictive Procedures," *Metall. Mater. Trans. B*, **28B**(4), pp. 651–663.